Electrochimica Acta 374 (2021) 137794

Contents lists available at ScienceDirect

Electrochimica Acta

journal homepage: www.elsevier.com/locate/electacta

Original Article

A dual NiCo metal-organic frameworks derived $NiCo_2S_4$ core-shell nanorod arrays as high-performance electrodes for asymmetric supercapacitors

Jiaxu Gong, Junxiao Yang, Jiaheng Wang, Linlin Lv, Wei Wang, Linyu Pu, Huan Zhang, Yatang Dai*

State Key Laboratory of Environment-friendly Energy Material, School of Materials Science and Engineering, Southwest University of Science and Technology, Mianyang 621010, PR China

ARTICLE INFO

Article history:
Received 13 November 2020
Revised 7 January 2021
Accepted 9 January 2021
Available online 14 January 2021

Keywords:
$NiCo_2S_4$
MOFs
Core-shell
Supercapacitor
Confine expansion

ABSTRACT

The structural stability of electrode materials is the crux of significantly improve the electrochemical performance of pseudocapacitor electrodes. Herein, we demonstrate the preparation of $NiCo_2S_4$ with core-shell and micro-porous structure on nickel foam as an efficient anode material for asymmetric supercapacitor (ASC) via hydrothermal and co-sulfurization processes. The $NiCo_2S_4$ electrode shows a remarkable specific capacitance of 850.2 C g^{-1} at 1 A g^{-1}, and retains 93.6 % original capacitance after 5000 cycles. Furthermore, the $NiCo_2S_4$ electrode also have excellent electrochemical performance when used as an anode of asymmetric $NiCo_2S_4$//Active Carbon (AC) supercapacitor, which generates an energy density as 38.1Wh Kg^{-1} at 700 W kg^{-1} and 84.3% capacity retention after 5000 cycles. This work provide an efficiently method to suppress volume expansion during sulfuration reaction by core-shell structure, which potential application in transition metal sulfides electrode materials in electrochemical energy storage and conversion devices.

1. Introduction

Owing to the excessive of energy consumption and environmental challenge, new systems for energy storage devices include lithium ion batteries (LIBs), solar cells and supercapacitors (SCs), have attracted substantial attentions [1–5]. Especially, SCs are served as an extraordinarily great performance device in many field including electronic products and powerplants due to its high power density, high power output, excellent stability and rapid rates in charge and discharge cycles [6–8]. According to energy storage mechanisms, SCs can be categorized as pseudocapacitors and electrical double layer capacitors (EDLCs) [9, 10]. ELDCs are based on the storage of electrostatic charge on the electrode surfaces, while pseudocapacitors are depend on redox reactions on the electrodes surface [11–13]. In general, the capacitance performance of most pseudocapacitors is better than that of EDLCs, which is benefiting from the fast reversible Faraday reaction occurred near the surface regions of the electrodes [14–16]. However, lower energy density limit the application of SCs in energy storage devices [17]. It can be raised energy density of the SCs through develop outstanding electrode materials with high energy density and constructing asymmetric supercapacitors (ASC) [18,19].

In the past decade, considerable efforts have been dedicated to exploring transition metal-based compounds, including transition metal oxides (TMOs) [20–22], transition metal hydroxides [23–25], transition metal selenides [26,27], and transition metal sulfides [28–31] are studied as effective electrode materials. In particular, transition metal sulfides are widely used as electrode materials in high performance ASC because of high electron transfer rates and rich reversible redox reaction active sites [32–34]. Recently, the research of nickel-cobalt binary-metal sulfides has been widely reported because of smaller band gap and better conductivity can offer high theoretical capacity [35]. Wang et al. reported that the $NiCo_2S_4$ nanosheets growth on nickel foam with the microwave method, which shows an excellent performance of 600.8 C g^{-1} (1502 F g^{-1}) at 1 A g^{-1} [19]. Dong et al. constructed $NiCo_2S_4$/grapheme composites electrode material for supercapacitors with shows an excellent performance of 455 C g^{-1} (910 F g^{-1}) at 1 A g^{-1} [36]. Huang et al. prepared hollow and spinous $NiCo_2S_4$ nanotubes use the natural silk as the template through a hydrothermal reaction, which shows a high specific capacitance of 346.5 C g^{-1} (630 F g^{-1}) at 1 A g^{-1} and still retained 91% after 3000 cycles [30]. In a nutshell, nickel-cobalt sulfides have good

* Corresponding author.
E-mail address: daiyt2003@163.com (Y. Dai).

https://doi.org/10.1016/j.electacta.2021.137794
0013-4686/

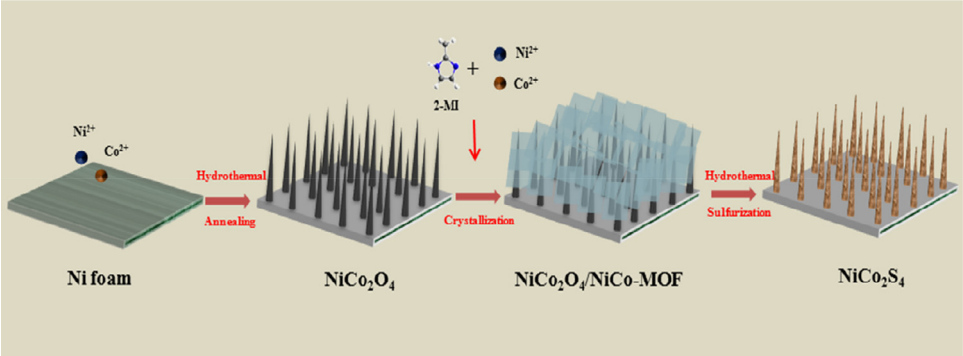

Scheme 1. Schematic illustration of synthetic process for NCS-A

conductivity and high specific capacitance showing great potential as energy storage materials.

Core-shell structure with highly ordered spatial structure, fast ion transport rate, and excellent structural stability are currently a favorable design in electrode materials [37–39]. Generally, the core of core-shell structure is usually designed as nanowires (or nanorods/nanospheres) and the shell is designed as nanosheets (or nanoparticles) to achieve better stable structure. Among the quantities of two-dimensional (2D) metal-based materials, the preparation of electrode materials using metal-organic frameworks (MOFs) as precursor has aroused much interest in recent year [40–42]. Although MOFs have high specific surface area, but most MOFs materials are unstable in acidic or alkaline electrolyte, even decompose to structural collapse. Therefore, many researchers use MOFs as a precursor for preparing metal-based materials, such as NiO [43], Co_3O_4 [44], Co_3S_4 [45], $CoMo_xO_y$ [46], $MnNi_2O_4$ [47].

In this work, we have successfully synthesized core-shell and micro-porous structure nickel cobalt sulfides, and use it as electrode materials in high-performance supercapacitors. The $NiCo_2O_4$ (named as NCO) nanowires were first synthesized by hydrothermal method due to the advantages of simple and easy control in the synthesis of metal oxides [48–50], and then NiCo-MOF nanosheets crystallization on the surface of the NCO nanoarrays, and $NiCo_2S_4$ nanorods are finally synthesized by a hydrothermal sulfurization method with a core-shell structure. The prepared $NiCo_2S_4$ electrode shows desirable electrochemical properties with 850.2 C g^{-1} at 1 A g^{-1}, while still retained 93.6% after 5000 cycles. Moreover, the as-prepared ASC made up of the $NiCo_2S_4$ electrode and active carbon (AC) shows an excellent specific capacity of 140 F g^{-1} at 1 A g^{-1} and energy density of 38.1 Wh kg^{-1} at 700 W kg^{-1}, as well as the remarkable cycling stability of 84.3% capacity retention after 5000 incessant cycles. This design demonstrating nickel cobalt sulfides with core-shell structure provides a novel strategy to improve electrochemical performance of $NiCo_2S_4$ and shows substantial potential uses for energy storage devices.

2. Results and discussion

The preparation procedure of $NiCo_2S_4$ is briefly exhibited in Scheme 1. First of all, the NCO nanowires arrays directly growth on the nickel foam (NF) by hydrothermal and annealed method based on previous reports [51]. Then the NCO is dipped into the NiCo-zeolitic imidazolate framework-67 (NiCo-ZIF-67) mixed solution, during this period Co^{2+} as a mental ion combined with 2-methylimidazole, while high concentrations of Ni^{2+} exchange part of Co^{2+} on Co-ZIF-67. The excessive Ni^{2+} can generate more H^+ during the hydrolytic process [52], prompted the Co-ZIF-67 three-dimensional structure turn into NiCo-MOF (named as NCM-A) nanosheets, which lead to the single nanosheets interconnected and formed a network-like structure on the surface of NCO nanowires (named as NCO/NCM-A). In addition, PTA was used as organic ligand for synthesized another kind of NiCo-MOF on the surface of NCO nanowires (named as NCO/NCM-B). In the final sulfuration reaction, the ion-exchange reactions occurred in NCO and NCM-A with S^{2-} ions. Because of the Kirkendall effect [53], the NCO nanowires expand outward results in internal microporous structure, and the NCM-A nanosheets contracted inward to form nanoparticles which confine excessive expansion of the $NiCo_2S_4$. In addition, the $NiCo_2S_4$ obtained by NCO, NCO/NCM-B, NCO/NCM-A (160 °C, 0.64 g Na_2S), NCO/NCM-A (140 °C, 0.64 g Na_2S), NCO/NCM-A (180 °C, 0.64 g Na_2S) NCO/NCM-A (160 °C, 0.48 g Na_2S) and NCO/NCM-A (160 °C, 0.8 g Na_2S) is named as NCS, NCS-B, NCS-A1, NCS-A2, NCS-A3, NCS-A4 and NCS-A5. Table S1 shows the detailed parameters in the synthesis of each sample.

SEM images of the resulting samples shown in Fig. 1, the results (Fig. 1a and 1d) indicate that the NCO nanowires arrays are vertical growth on the NF. Enlarged SEM image of nanowires shows uniform distribution and smooth surface, with the diameter of a single NCO nanowire is about 40 nm. After the NCM-A nanosheets crystallized on the NCO nanowires, as shown in Fig. 1b and 1e. The NCM-A nanosheets complete coverage on every NCO nanowires, and the unique nanosheets could form on the nanowires under the mild reaction conditions benefit from NiCo-ZIF-67, which different from using PTA as ligand that grow directly into nanoparticles on nanowires. In order to further understand the NCM formed by the two ligands. The NCM-A and NCM-B directly grew in the NF (Fig. S1), both of them grew as nanosheets, but NCM-B is much larger and even nanoparticles can be observed at high magnification. During crystallization on NCO nanowires, influenced by preferential reduction of surface energy, the small size of NCM-A forms interconnected nanosheets, while the NCM-B tends to form nanoparticles as Fig. S2.

The NCS-A1 was prepared through hydrothermal sulfuration (Fig. 1c and 1f), NCO/NCM-A nanowires/nanosheets structure disappeared and became rough nanowires coated with nanoparticles. The single NCS-A1 nanowire is about 80 nm and vertical growth on the NF with formed a core-shell structure. The effect of sulfuration reaction temperature on morphology can clearly observe from the SEM images of NCS-A2 and NCS-A3 (Fig. S3). At low temperature the sulfuration reaction rate was reduced and S^{2-} ions diffusion was slower, which may lead to more S^{2-} ions aggregated nearly the heterogeneous surface formed by the NF and the nanorods, and promoted over-sulfuration at the connection site between the NF and the nanorods. This causes the nanorods fractured from the bottom and no longer be vertical. While high temperature lead to rapid disintegration of nanorods into nanoparticles and massive agglomeration to collapsed the structure. Different dosage of Na_2S were affected the sample size, which can observe from the SEM images of NCS-A4 and NCS-A5 (Fig. S4). The diameter of nanowires

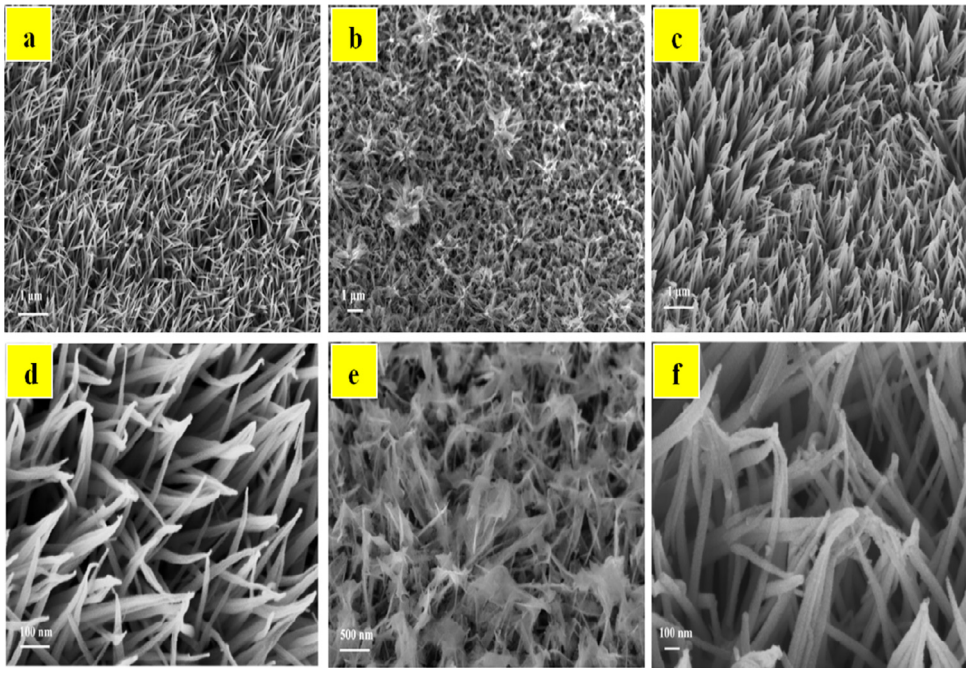

Fig. 1. SEM images of (a, d) NCO. (b, e) NCO/NCM-A. (c, f) NCS-A1.

increased from about 50 nm to about 150 nm with the increased of dosage of Na_2S. The increase of the dosage of Na_2S leads to a higher concentration of sulfide ions released during the reaction, and the Kirkendall effect in the formation of Ni-Co sulfide with metal ions becomes more obvious, and the diameter of nanorods increases [54,55]. The surface of NCS-B nanowires (Fig. S5a and 5b) is smoother than that of NCS-A, which may due to the outward expansion of NCO during sulfuration leads to the shed of some NCM-B nanoparticles with larger size. While the SEM images of NCS are shown in Fig. S5c and 5d.

Furthermore, the TEM and HRTEM images of NCO/NCM-A and NCS-A1 are shown in Fig. 2. The TEM images of NCO/NCM-A (Fig. 2a) clearly indicated that the multiple NCO nanowires were coated with NCM-A nanosheets. Due to the ultrasonic dispersion of the samples before TEM testing, some of the nanosheets on the top of the nanowires fell off, and exposed smooth NCO nanowires. The NCO nanowires (Fig. 2b) with a diameter of 45 nm are composed of nanoparticles compactly forming. Fig. 2c showed that NCS is composed by NCO core and NCM-A shell, which together constituted NCS-A1 nanorods with a core-shell structure, and the diameter about 85 nm. It is worth noting that unlike NCO nanowires are tightly stacked by nanoparticles, NCS-A1 appeared micro-porous structure both in the core and shell, which provides more efficient ions transport channel [56]. HRTEM images of NCS-A1 as shown in Fig. 2d that calculated lattice spacing of 0.23 nm is indexed to the (400) plane of $NiCo_2S_4$. The results of HRTEM analysis further confirmed the excellent crystallinity of NCS-A1. In addition, the uniform distribution of Ni, Co and S elements on the surface of the example was further verified by EDS spectral mapping images (Fig. 2e-h). Meanwhile, the EDS plot of NCO/NCM-A and NCS-A1 are shown in Fig. S6 and S7.

The phase structures of composites, is confirmed by the XRD patterns (Fig. 3a). For pristine NCO, all diffraction peaks are well indexed to the $NiCo_2O_4$ phase (PDF#20-0781) [57], except for the peaks arising from the nickel foam which marked by "*". The diffraction peak of NCM was not observed in XRD pattern due to its low crystallinity. After sulfuration reaction, the $NiCo_2O_4$ diffraction peaks disappeared and new diffraction peaks appeared in all samples with the peak positions were indexed to the $NiCo_2S_4$ phase (PDF#20-0782) [58]. Moreover, the XRD patterns of NCM-B and NCO/NCM-B as shown in Fig. S8.

The FT-IR spectra of NCO, NCO/NCM-A, NCS-A1, NCS samples are shown in Fig. 3b. Two characteristic peaks at 3399 cm^{-1} and 1626 cm^{-1} attributed to the hydrogen-bonded hydroxyl groups stretching vibration in the samples. The peaks at 661 cm^{-1} and 555 cm^{-1} attributed to the M–O bonds (M means Ni or Co) with stretching and bending in the $NiCo_2O_4$ [3, 59]. The peak at 1085 and 2925 cm^{-1} attributed to the imidazole ring stretching and bending vibration, and the aromatic nucleus in 2-Methylimidazole vibration in the NCO/NCM-A, respectively [60]. From NCS-A1 and NCS spectra, the new peaks emerge at 1101 (or 1061) and 630 (or 580) cm^{-1} after sulfuration reaction attributed to the S=O and the M–S (M means Ni or Co) with stretching and bending, respectively.

The complete XPS spectrum of the NCS-A1 sample (Fig. 3c) includes Ni 2p, Co 2p, S 2p. The O element can be attributed to water molecules absorbed on the sample surface and the C element may be intervention of CO_2 or organics. Ni 2p spectrum is showed in Fig. 3d, two shakeup satellites denoted as "Sat" and two major intensive peaks exhibited at 855.9 and 873.3 eV are in accordance with Ni $2p_{3/2}$ and Ni $2p_{1/2}$, which confirming the presence of Ni^{2+} cations [61,62]. Similarly, Co 2p spectrum (Fig. 3e) shows that the peaks of 780.7 and 796.5 eV correspond to Co^{2+}, while the peaks of 778.5 and 793.8 eV correspond to Co^{3+}, which indicate the coexistence of Co^{2+} and Co^{3+} [63]. The S 2p XPS spectra were showed in Fig. 3f, the intensive peaks of 161.2 and 162.2eV belong to S $2p_{3/2}$ and $2p_{1/2}$ levels, and the satellite peak at 168.3eV reveals the partially oxidized on surface of sulphur ions [64]. Based on the above results of SEM, HRTEM, XRD, FT-IR, and XPS, it can be concluded that the $NiCo_2S_4$ nanorods with a core-shell structure have been successfully synthesized.

Subsequently, the cyclic voltammetry (CV) curves of NF, NCO, NCO/NCM-A, NCS and NCS-A1 at a scan rate of 10 mV s^{-1} and across a voltage window of 0 to 0.6 V were showed in the Fig. 4a. The contribution of bare NF to the capacitance can be ignored. Obviously, NCS-A1 electrode has larger integral area and

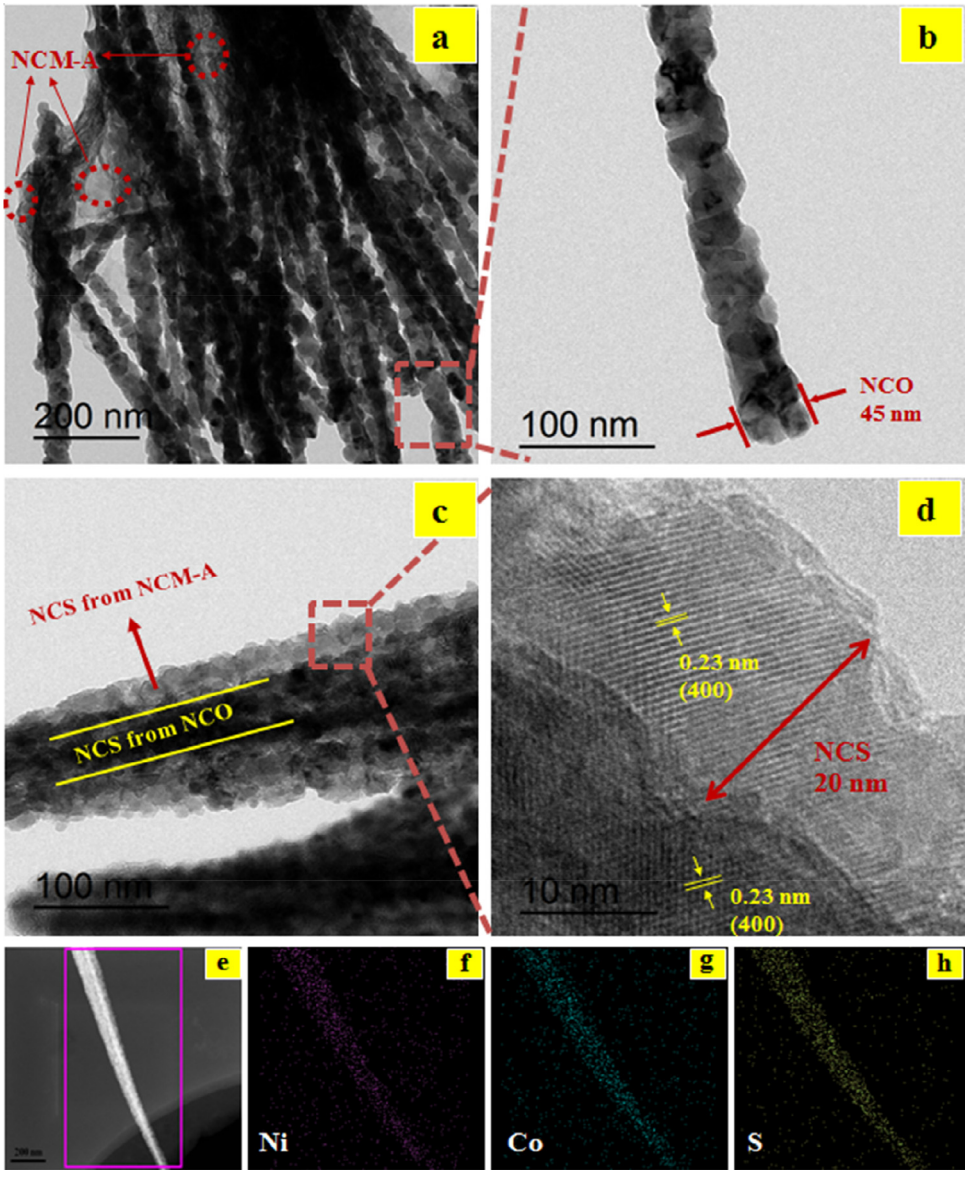

Fig. 2. TEM images of (a, b) NCO/NCM-A and (c) NCS-A1. (d) HRTEM image and (e)-(h) EDS spectral mapping images of NCS-A1.

higher specific capacitance. Similarly, the CV curves of NCS-A under the different vulcanization conditions and NCS-B were showed in Fig. 4b. Several peaks of redox reaction indicated that the pseudo-capacitance feature of Faraday redox reaction. The relevant equations as follow [36, 65]:

$$NiCo_2S_4 + 2OH^- \leftrightarrow 4NiS_{2x}OH + Co_2S_{4-2x}OH + 2e^- \quad (1)$$

$$Co_2S_{4-2x}OH + 3OH^- \leftrightarrow 2CoS_{2-x}O + 2H_2O + 3e^- \quad (2)$$

The magnitude order of the integral area with the CV curves of the electrodes is NCS-A1> NCS-B> NCS-A2> NCS-A4> NCS-A5> NCS-A3. The electrochemical performances of those electrodes are presented in Fig. S9 and S10. The CV curves of the NCS-A1 at different scanning rates are also shown in Fig. 4c. Excellent redox properties in electrochemical of NCS-A1 attribute to the superiority of the core-shell structure and micro-porous structure, which can accelerate the penetration of OH^- ions into the electrode and increase the number of active sites. To further quantify the numbers of electrochemical active sites in those electrodes, the active sites were calculated from the voltammetric charge (The calculation formulas in the Supporting Information) and shown in Fig. S11. The NCS-A1 has 2.55 times more active sites than NCO and 1.68 times more active sites than NCS at a scan rate of 10 mV s^{-1} from the CV measurement. This results directly show that the unique structure with core-shell and micro-porous can enhance the number of active sites to improve the electrochemical properties.

The specific capacities of the samples are calculated from the GCD with the voltage of 0-0.4 V in Fig. 4d-f. The formula for calculated specific capacitances is given in Support Information. The specific capacitances at current density of 1 A g^{-1} with NCO, NCO/NCM-A, NCS, NCS-B, NCS-A1, NCS-A2, NCS-A3, NCS-A4 and NCS-A5 are 356.5, 406, 619, 794.9, 850.2, 620, 297, 445 and 412.6 C g^{-1}, respectively. The specific capacity of NCS-A3 is even lower than that of the original NCO, which possibly due to the structure complete collapsed at high sulfuration temperature. For NCS-A4 and NCS-A5, oversized nanorods are more prone to structural collapse during electrochemical oxidation and reduction, resulting in performance degradation. As similarly as shown in the CV curve, NCS-A1 electrodes also represent the best electrochemical performance compared with others electrodes in the GCD test. The specific capacitances of NCS-A1 are 850.2, 774.2, 733.3, 687 and 593

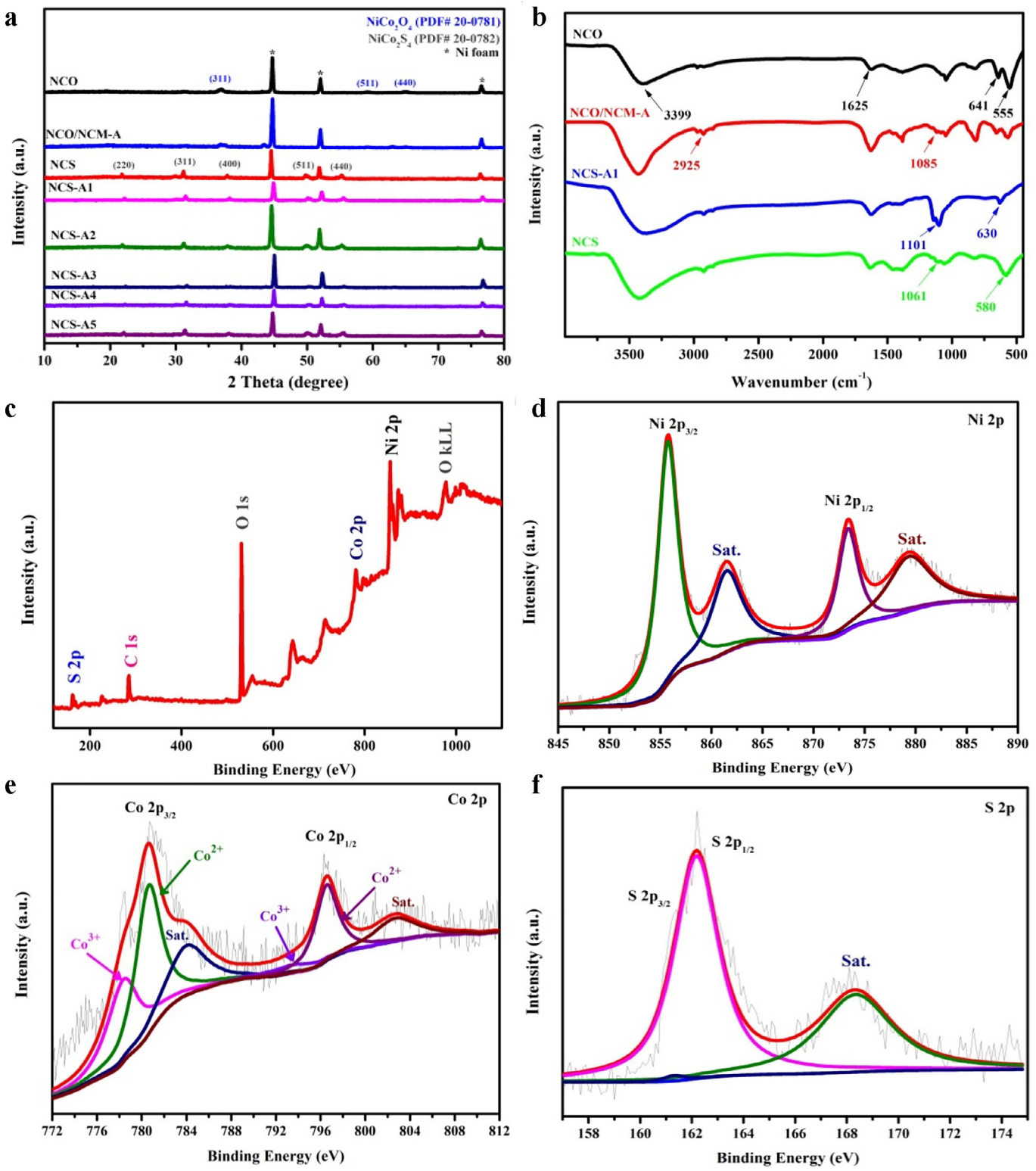

Fig. 3. (a) XRD pattern of samples. (b) FT-IR spectra of samples. XPS spectra of (c) the survey spectrum, (d) Ni 2p, (e) Co 2p and (f) S 2p of NCS-A1.

C g^{-1} at the current density of 1, 2, 3, 5and 10 A g^{-1}, respectively. The cyclic stability performance of NCS-A1 (Fig. 4g) suggesting an outstanding rate capability, which still delivers 69.7% of capacitance at 10 A g^{-1}.

The electrochemical impedance spectroscopy (EIS) was showed in Fig. 4h. After fitting with an equivalent circuit, EIS results of the samples with charge transfer resistance (Rct) and equivalent series resistance (Rs) are summarized in Table S2. It is observed that Rct and Rs values of the NCS-A1 were 0.09 Ω and 0.55 Ω, respectively. Compared with other electrodes, NCS-A1 has lower Rs and Rct, which due to its excellent electrical conductivity, and also observed the line in the low frequency region that is almost parallel to the Y-axis indicates the fast ions diffusion at the NCS-A1/KOH aqueous interface. Meanwhile, all of the nickel cobalt sulfides except

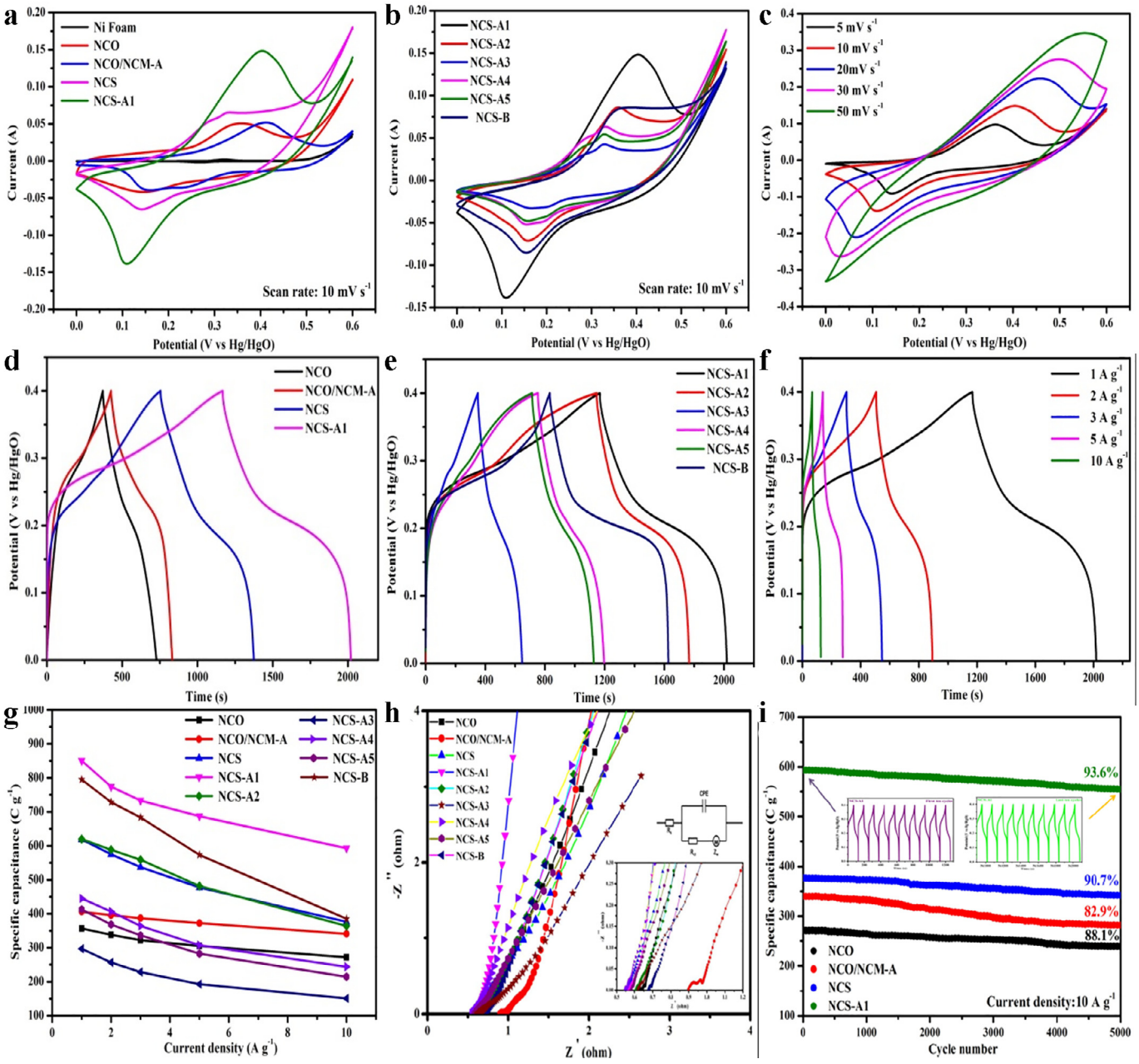

Fig. 4. (a) CV curves at 10 mV s^{-1} and (d) GCD curves at 1 A g^{-1} of the NF (without GCD curves), NCO, NCO/NCM-A, NCS and NCS-A1 samples. (b) CV curves at 10 mV s^{-1} and (e) GCD curves at 1 A g^{-1} of the NCS-A1, NCS-A2, NCS-A3, NCS-A4, NCS-A5 and NCS-B samples. (c) CV curves and (f) GCD curves at various current densities of NCS-A1. (g) Specific capacity versus current density plots of all samples. (h) EIS spectra of all samples (the insets shows the equivalent circuit diagram and the plots in high frequency region). (i) Cyclic stability of the NCO, NCO/NCM-A, NCS, NCS-A1 at 10 A g^{-1} (the inset shows first and final ten GCD cycles of NCS-A1).

for the NCS-A3 exhibit lower internal resistance than NCO, which may cause of the micro-porous structure can improved OH^- ions transfer rate in the electrodes after sulfurization. The NCS-A1 electrode also exhibits excellent cycling stability (Fig. 4i). Remarkably, NCS-A1 electrode shows the retention rate of capacity is 93.6 % at a current density of 10 A•g^{-1} after 5000 cycles, while the capacity retention rate is 88.1%, 82.9 % and 90.7 % for NCO, NCO/NCM and NCS electrode, respectively. The inset in the Fig. 4i shows first and final ten charge-discharge cycles of NCS-A1 electrode with outstanding cyclical stability and rate capability. Such excellent cycling stability is mainly attributed to the unique structure design of NCS-A1, which the $NiCo_2S_4$ nanoparticles coated on $NiCo_2S_4$ nanorods can enable competently house buffer structural changes and prevent collapse of the materials. On the other hand, core-shell structure can shorten the length of electrolyte ion transport and improve the cycle stability. The NCS-A1 in this work shows the excellent electrochemical performance comparing with the previously reported researches which about transition metal chalcogenides-based electrode materials (in Table S3). It is not only superior to most of the $NiCo_2S_4$ electrode materials, but also be competitive in the composite of metal sulfide compound with some high conductivity carbon materials.

In order to further investigate the utilization value of the NCS-A1 electrode material, the ASC device was fabricated using NCS-A1 electrode as the cathode and AC coated on nickel foam as the anode with 3 M KOH electrolyte, which denoted as NCS-A1//AC, and as schematically illustrated in Fig. 5a. In addition, the electrochemical performances of the AC electrode are showed in Fig.

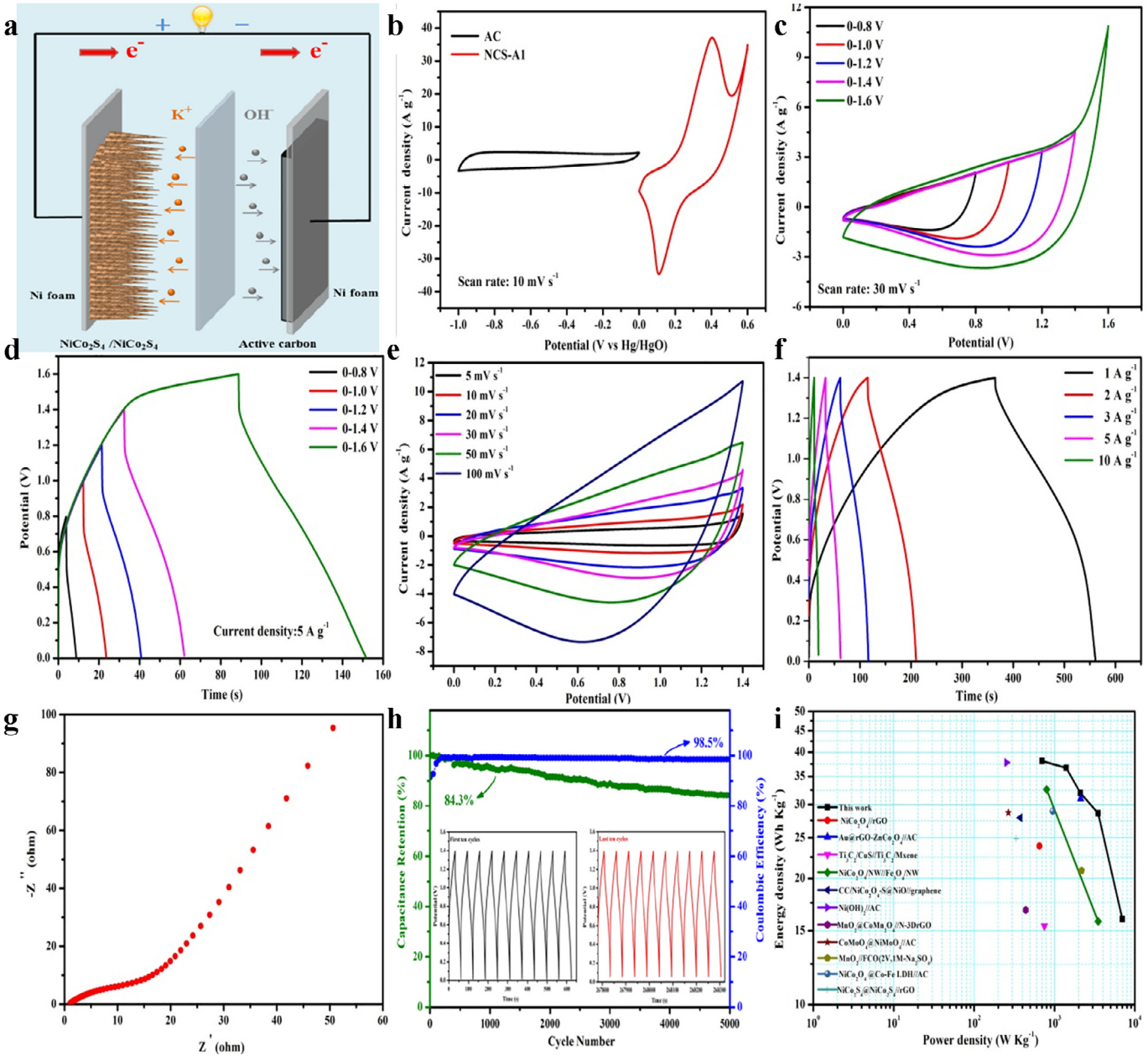

Fig. 5. (a) Schematic diagram of the assembled NCS-A1//AC device. (b) CV curves of NCS-A1 and AC at 10 mV s^{-1}. (c) CV curves of ASC device at different potential with a scanning rate of 30 mV s^{-1}. (d) GCD curves of ASC device under different potential windows, (e) CV curves of the ASC device at different scan rates. (f) GCD curves of the ASC device at different current densities. (g) Nyquist plot of the ASC. (h) Capacitance retention and Coulombic efficiency of ASC device at 5 A g^{-1} (the inset shows first and final ten GCD cycles. (i) Ragone plots of ASC device.

S13. CV measurements in 30 mV s^{-1} for both positive and negative (Fig. 5b) indicated that the feasibility of working potential window can be get to 1.6 V, which based on the working potential window of NCS-A cathode electrode complementary to AC anode electrode. A series of CV and GCD measurements at various voltages from 0.8 to 1.6 V were used to tested the NCS-A1//AC device for determined a stable potential window. As the working voltage increased to 1.6 V, the CV curve appears a conspicuous polarization due to the water splitting (Fig. 5c), while the symmetric of GCD curve has changed significantly (Fig. 5d). Thus, the stable working voltage window of 1.4 V was used to study the electrochemical properties of ASC.

The CV curves of ASC are showed in Fig. 5e. GCD measurements carried out over different current density are showed in Fig. 5f, and the specific capacitances of NCS-A1//AC device are 140, 134.9, 117.4, 105 and 58.6 F g^{-1} at the current density of 1, 2, 3, 5and 10 A g^{-1}, respectively. Moreover, the Nyquist plot of ASC (Fig. 5g) shows lower internal resistance, which means faster of ions diffusion rate. The cycling performance of NCS-A1//AC device (Fig. 5h) at a current density of 5 A g^{-1} for 5000 cycles. With the charge-discharge after about 150 cycles, the electrodes are fully activated, and the Coulombic efficiency reach up to 99.2%. As seen, the device exhibits excellent cycling stability, which specific capacitance retention can reach to 84.3% and Coulombic efficiency can also achieved nearly 98.5% after 5000 cycles. The inset in the Fig. 5h shows first and final ten charge-discharge cycles of NCS-A1//AC device with outstanding cyclical stability and rate capability. As shown in Fig. 5i, the energy density and power density of NCS-A1//AC were calculated from GCD curves (the calculation formulas in the Supporting Information). The energy den-

sity are 38.1, 36.7, 32, 28.6 and 16 Wh kg^{-1} at the power density of 700, 1400, 2100, 3500 and 7000 W kg^{-1}, which is superior to the previously reported researches about materials based on TMOs or TMCs, such as $NiCo_2O_4$//rGO (23.9 Wh kg^{-1} at 650 W kg^{-1}) [66], Au@rGO-$ZnCo_2O_4$//AC (31 Wh kg^{-1} at 2121 W kg^{-1}) [67], Ti_3C_2/CuS//Ti_3C_2/Mxene (15.4 Wh kg^{-1} at 750.2 W kg^{-1}) [68], $NiCo_2O_4$/Ni wire//Fe_3O_4/Ni wire (32.6 Wh kg^{-1} at 800 W kg^{-1} and 15.8 Wh kg^{-1} at 3500 W kg^{-1}) [69], CC/$NiCo_2O_4$-S@NiO//graphene (27.9 Wh kg^{-1} at 375 W kg^{-1}) [70], $Ni(OH)_2$//AC (37.8 Wh kg^{-1} at 252.67 W kg^{-1}) [71], MnO_2@$CoMn_2O_4$//N-3DrGO (16.82 Wh kg^{-1} at 440 W kg^{-1}) [72], $CoMoO_4$@$NiMoO_4$//AC (28.7 Wh kg^{-1} at 267 W kg^{-1}) [73], MnO_2//FCO (20.89 Wh kg^{-1} at 2173.9 W kg^{-1}) [74], $NiCo_2O_4$@Co-Fe LDH//AC (28.94 Wh kg^{-1} at 950 W kg^{-1} and 18.47 Wh kg^{-1} at 4925 W kg^{-1}) [75], $NiCo_2S_4$@$NiCo_2S_4$//rGO (24.9 Wh kg^{-1} at 334 W kg^{-1} and 12.6 Wh kg^{-1} at 2444 W kg^{-1}) [76]. More information on the performance of NCS-A1//AC devices compared to previously reported supercapacitors is listed in Table S4.

Based on all the electrochemical results above, the NCS-A1 electrode exhibits excellent electrochemical performance as an anode in ASC, which due to its unique internal structure. In this core-shell structure, the $NiCo_2S_4$ core layer formed after sulfidation has a large number of micro-pores inside, which increased the contact space between electrolyte and material, and significantly improved the number of active sites while enhanced the capacity performance of the material. Meanwhile, the $NiCo_2S_4$ shell layer after sulfidation which based on the NiCo-ZIF-67 under the appropriate reaction conditions that makes the electrode material maintain its capacity, which in the way of slow down the volume expansion generated in the long-term charge-discharge cycle for improve the cycling stability. In summary, the NCS-A1 electrode material with core-shell structure has excellent electrochemical performance and broad application prospect when used as an anode for high performance asymmetric supercapacitors.

4. Conclusions

In summary, we have successfully synthesized core-shell structure $NiCo_2S_4$ arrays on Ni foam as an efficient positive electrode material for ASC via multi-step hydrothermal and co-sulfuration processes. It was found that the $NiCo_2S_4$ nanorods formed by sulfuration of the NiCo-ZIF-67 nanosheets under optimized conditions, which can effectively confine the volume expansion produced by NCO during sulfuration reaction and formed a stable core-shell structure. Moreover, a mass of micro-pores appear in internal structure can provide more active sites for charge transfer and achieve higher specific capacitance. The $NiCo_2S_4$ electrode shows a remarkable specific capacitance of 850.2 C g^{-1} at the current density of 1 A g^{-1} and retains 93.6 % original capacitance after 5000 cycles at a current density of 10 A g^{-1}. Furthermore, the $NiCo_2S_4$ electrode also achieved the excellent electrochemical performance when used as an anode of asymmetric $NiCo_2S_4$//AC supercapacitor, which delivers an energy density as 38.1Wh Kg^{-1} at 700 W kg^{-1}, and as well as the remarkable cycling stability of 84.3% capacity retention after 5000 incessant cycles. This work would provide a simplify and efficiently method to obtain the core-shell structure which can confine the excessive volume expansion during the sulfuration reaction, and it can be further apply to others transition metal sulfides electrode materials in electrochemical energy storage and conversion devices.

Declaration of Competing Interest

The authors declare that they have no known competing financial interests or personal relationships that could have appeared to influence the work reported in this paper.

Credit authorship contribution statement

Jiaxu Gong: Conceptualization, Writing - original draft. **Junxiao Yang:** Supervision, Validation. **Jiaheng Wang:** Supervision. **Linlin Lv:** Data curation, Investigation. **Wei Wang:** Investigation, Formal analysis. **Linyu Pu:** Writing - review & editing, Software. **Huan Zhang:** Supervision. **Yatang Dai:** Project administration, Funding acquisition, Resources.

Acknowledgments

This work was supported by the Open Project of State Key Laboratory of Environment-friendly Energy Materials (18FKSY0207) and Southwest University of Science and Technology Longshan Academic Talent Research Support Program (18LZX403).

Supplementary materials

Supplementary material associated with this article can be found, in the online version, at doi:10.1016/j.electacta.2021.137794.

References

[1] C.G. Wang, E. Zhou, W.D. He, X.L. Deng, J.Z. Huang, M. Ding, X.Q. Wei, X.J. Liu, X.J. Xu, $NiCo_2O_4$-based supercapacitor nanomaterials, Nanomaterials 7 (2017) 41, doi:10.3390/nano7020041.
[2] M.H. Yu, Y.C. Huang, C. Li, Y.X. Zeng, W. Wang, Y. Li, P.P. Fang, X.H. Lu, Y. X, Building three-dimensional graphene frameworks for energystorage and catalysis, Adv. Funct. Mater. 25 (2015) 14, doi:10.1002/adfm.201402964.
[3] X.Q. Dai, Y.T. Dai, J.H. Lu, LY. Pu, W. Wang, J. Jin, F. Ma, N. Tie, Cobalt oxide nanocomposites modified by nico-layered double hydroxide nanosheets as advanced electrodes for supercapacitors, Ionics 26 (2019) 18, doi:10.1007/s11581-019-03333-6.
[4] R. Kotz, M. Carlen, Principles and applications of electrochemical capacitors, Electrochim. Acta. 45 (2000) 2483–2498, doi:10.1016/S0013-4686(00)00354-6.
[5] Y. Sun, P. Ma, L. Liu, J. Chen, X. Zhang, J. Lang, X. Yan, Solar-Thermal Driven Self-Heating of Micro-Supercapacitors at Low Temperatures, Sol. RRL. 2 (2018) 1800223, doi:10.1002/solr.201800223.
[6] P. Simon, Y. Gogotsi, B. Dunn, Where do batteries end and supercapacitors begin, Science 343 (2014) 1210–1211, doi:10.1126/science.1249625.
[7] J.R. Miller, P. Simon, Electrochemical capacitors for energy management, Science 321 (2008) 651–652, doi:10.1126/science.1158736.
[8] M. Aneke, M. Wang, Energy storage technologies and real life applications-A state of the art review, Appl. Energ. 179 (2016) 350–377, doi:10.1016/j.apenergy.2016.06.097.
[9] Y. Zhai, Y. Dou, D. Zhao, P.F. Fulvio, R.T. Mayes, S. Dai, Carbon materials for chemical capacitive energy storage, Adv. Mater. 23 (2011) 4828–4850, doi:10.1002/adma.201100984.
[10] B.L. Ellis, K. Philippe, D. Thierry, Three-dimensional self-supported metal oxides for advanced energy storage, Adv. Mater. 45 (2014) 3368–3397, doi:10.1002/adma.201306126.
[11] M. Inagaki, H. Konno, O. Tanaike, Carbon materials for electrochemical capacitors, J. Power. Sources. 195 (2010) 7880–7903, doi:10.1016/j.jpowsour.2010.06.036.
[12] J. Yan, Q. Wang, T. Wei, Z.J. Fan, Recent advances in design and fabrication of electrochemical supercapacitors with high energy densities, Adv. Energy. Mater. 4 (2014) 1300816, doi:10.1002/aenm.201300816.
[13] X. Wang, J. Ding, S. Yao, X. Wu, Q. Feng, Z. Wang, B. Geng, High supercapacitor and adsorption behaviors of flower-like MoS_2 nanostructures, J. Mater. Chem. A. 2 (2014) 15958–15963, doi:10.1039/C4TA03044C.
[14] Y. Yang, S. Li, W. Huang, H.G. Shang, C. Engelbrekt, S. Duan, P. Si, Effective synthetic strategy for $Zn_{0.76}Co_{0.24}S$ encapsulated in stabilized N-doped carbon nanoarchitecture towards ultra-long-life hybrid supercapacitors, J. Mater. Chem. A. 7 (2019) 14670–14680, doi:10.1039/C9TA03575C.
[15] H. Wang, Q. Ren, D.J. Brett, G. He, R. Wang, J. Key, S. Ji, Double-shelled tremella-like NiO@ Co_3O_4@MnO_2 as a high-performance cathode material for alkaline supercapacitors, J. Power. Sources 343 (2017) 76–82, doi:10.1016/j.jpowsour.2017.01.042.
[16] F. Ma, X.Q. D, J. Jin, N. T, Y.T. Dai, Hierarchical core-shell hollow $CoMoS_4$@Ni-Co-S nanotubes hybrid arrays as advanced electrode material for supercapacitors, Electrochim. Acta 331 (2020) 135459, doi:10.1016/j.electacta.2019.135459.
[17] Y. Huang, Y. Zeng, M. Yu, P. Liu, Y. Tong, F. Cheng, X. Lu, Recent smart methods for achieving high-energy asymmetric supercapacitors, Small Methods 2 (2018) 1700230, doi:10.1002/smtd.201700230.
[18] S. Chen, S. Cui, S. Chandrasekaran, C. Ke, Z. Li, P. Chen, C. Zhang, Y. Jiang, Growth of $CuCo_2O_4$@$MnMoO_4$ core/shell nanosheet arrays for high energy density asymmetric supercapacitors, Electrochim. Acta 341 (2020) 135893, doi:10.1016/j.electacta.2020.135893.

[19] F. Wang, G. Li, J. Zheng, J. Ma, C. Yang, Q. Wang, Microwave synthesis of three-dimensional nickel cobalt sulfide nanosheets grown on nickel foam for high-performance asymmetric supercapacitors, J. Colloid. Interf. Sci. 516 (2018) 48–56, doi:10.1016/j.jcis.2018.01.038.

[20] L. Hu, L. Wu, M. Liao, X. Hu, X. Fang, Electrical transport properties of large, individual $NiCo_2O_4$ nanoplates, Adv. Funct. Mater. 22 (2012) 998–1004, doi:10.1002/adfm.201102155.

[21] Z. Qu, M. Shi, H. Wu, Y. Liu, J. Jiang, C. Yan, An efficient binder-free electrode with multiple carbonized channels wrapped by $NiCo_2O_4$ nanosheets for high-performance capacitive energy storage, J. Power. Sources 410 (2019) 179–187, doi:10.1016/j.jpowsour.2018.11.018.

[22] G. Chen, Y. Yang, Y. Dai, W. Wang, Preparation of high-capacity carbon-coated nickel cobaltate hollow nanospheres electrode for supercapacitors, Int. J. Electrochem. Sci. 15 (2020) 5342–5351, doi:10.20964/2020.06.43.

[23] H. Chen, L. Hu, Y. Yan, R. Che, M. Chen, L. Wu, One-step fabrication of ultrathin porous nickel hydroxide-manganese dioxide hybrid nanosheets for supercapacitor electrodes with excellent capacitive performance, Adv. Energy. Mater. 3 (2013) 1636–1646, doi:10.1002/aenm.201300580.

[24] J. Huang, P. Xu, D. Cao, X. Zhou, S. Yang, Y. Li, Wang G, Asymmetric supercapacitors based on β-$Ni(OH)_2$ nanosheets and activated carbon with high energy density, J. Power. Sources 246 (2014) 371–376, doi:10.1016/j.jpowsour.2013.07.105.

[25] X Wu, M Lian, Q Wang, A High-performance, Asymmetric Supercapacitors based on Hydrogen bonding Nanoflower-like Polypyrrole and $NiCo(OH)_2$ electrode materials, Electrochim. Acta 295 (2019) 655–661, doi:10.1016/j.electacta.2018.10.199.

[26] F. Ma, J. Lu, L. Pu, W. Wang, Y. Dai, Construction of hierarchical cobalt-molybdenum selenide hollow nanospheres architectures for high performance battery-supercapacitor hybrid devices, J. Colloid. Interf. Sci. 563 (2020) 435–446, doi:10.1016/j.jcis.2019.12.101.

[27] S. Wang, W. Li, L. Xin, M. Wu, Y. Long, H. Huang, X. Lou, Facile synthesis of truncated cube-like $NiSe_2$ single crystals for high-performance asymmetric supercapacitors, Chem. Eng. J. 330 (2017) 1334–1341, doi:10.1016/j.cej.2017.08.078.

[28] F. Huang, R. Meng, Y. Sui, F. Wei, J. Qi, Q. Meng, Y. He, One-step hydrothermal synthesis of a CoS_2@MoS_2 nanocomposite for high-performance supercapacitors, J. Alloy. Comp. 742 (2018) 844–851, doi:10.1016/j.jallcom.2018.01.324.

[29] Y. Li, J. Chen, Y. Ji, W. Yang, X.Z. Fu, R. Sun, C.P. Wong, Hierarchical graphite foil/$CoNi_2S_4$ flexible electrode with superior thermal conductivity for high-performance supercapacitors, J. Energy. Chem. 27 (2018) 463–471, doi:10.1016/j.jechem.2017.11.016.

[30] W. Huang, A. Zhang, H. Liang, R. Liu, J. Cai, L. Cui, J. Liu, Novel fabrication of hollow and spinous $NiCo_2S_4$ nanotubes templated by natural silk for all-solid-state asymmetric supercapacitors, J. Colloid. Interf. Sci. 549 (2019) 140–149, doi:10.1016/j.jcis.2019.04.066.

[31] C. Chen, J. Zhou, Y. Li, Q. Li, K. Tao, L. Han, Mesoporous Ni_2CoS_4 electrode materials derived from coordination polymer bricks for high-performance supercapacitor, J. Solid. State. Chem. 271 (2019) 239–245, doi:10.1016/j.jssc.2018.12.060.

[32] X.Y. Yu, X.W. Lou, Mixed metal sulfides for electrochemical energy storage and conversion, Adv. Energy. Mater. 8 (2018) 1701592, doi:10.1002/aenm.201701592.

[33] B.Y. Guan, L. Yu, X. Wang, S. Song, X.W. Lou, Formation of onion-like $NiCo_2S_4$ particles via sequential ion-exchange for hybrid supercapacitors, Adv. Mater. 29 (2017) 1605051, doi:10.1002/adma.201605051.

[34] J. Yang, C. Yu, X. Fan, S. Liang, S. Li, H. Huang, Z. Ling, C. Hao, J. Qiu, Electroactive edge site-enriched nickel–cobalt sulfide into graphene frameworks for high-performance asymmetric supercapacitors, Energ. Environ. Sci. 9 (2016) 1299–1307, doi:10.1039/C5EE03633J.

[35] W. Hong, J. Wang, Z. Li, S. Yang, Fabrication of Co_3O_4@Co-Ni sulfides core/shell nanowire arrays as binder-free electrode for electrochemical energy storage, Energy 93 (2015) 435–441, doi:10.1016/j.energy.2015.09.053.

[36] M. Dong, Z. Wang, G. Yan, J. Wang, H. Guo, X. Li, Confine growth of $NiCo_2S_4$ nanoneedles in graphene framework toward high-performance asymmetric capacitor, J. Alloy. Comp. 822 (2020) 153645, doi:10.1016/j.jallcom.2020.153645.

[37] S. Liu, K. San Hui, K.N. Hui, J.M. Yun, K.H. Kim, Vertically stacked bilayer $CuCo_2O_4$/$MnCo_2O_4$ heterostructures on functionalized graphite paper for high-performance electrochemical capacitors, J. Mater. Chem. A. 4 (2016) 8061–8071, doi:10.1039/C6TA00960C.

[38] W. Xiong, X. Hu, X. Wu, Y. Zeng, B. Wang, G. He, Z. Zhu, A flexible fiber-shaped supercapacitor utilizing hierarchical $NiCo_2O_4$@polypyrrole core-shell nanowires on hemp-derived carbon, J. Mater. Chem. A. 3 (2015) 17209–17216, doi:10.1039/C5TA04201A.

[39] Y. Zhao, X. He, R. Chen, Q. Liu, J. Liu, D. Song, H. Zhang, H. Dong, R. Li, M. Zhang, J. Wang, Hierarchical $NiCo_2S_4$@$CoMoO_4$ core-shell heterostructures nanowire arrays as advanced electrodes for flexible all-solid-state asymmetric supercapacitors, Appl. Surf. Sci. 453 (2018) 73–82, doi:10.1016/j.apsusc.2018.04.159.

[40] D.P. Dubal, K. Jayaramulu, J. Sunil, S. Kment, P. Gomez-Romero, C. Narayana, R. Zboril, R.A. Fischer, Metaleorganic framework (MOF) derived electrodes with robust and fast lithium storage for Li-ion hybrid capacitors, Adv. Funct. Mater. 29 (2019) 1900532, doi:10.1002/adfm.201900532.

[41] S. Liu, D. Li, G. Zhang, D. Sun, J. Zhou, H. Song, Two-Dimensional $NiSe_2$/N-rich carbon nanocomposites derived from Ni-hexamine frameworks for superb Na-ion storage, ACS Appl. Mater. Interfaces 10 (2018) 34193–34201, doi:10.1021/acsami.8b10635.

[42] Y. Yasun, Upendra.A. Kannangara, Jang-Kun.Song Rathnayake, Hybrid supercapacitors based on metal organic frameworks using p-phenylenediamine building block, Chem. Eng. J. 361 (2019) 1235–1244, doi:10.1016/j.cej.2018.12.173.

[43] H. Yin, J. Zhu, J. Chen, J. Gong, Q. Nie, MOF-derived in situ growth of carbon nanotubes entangled Ni/NiO porous polyhedrons for high performance glucose sensor, Mater. Lett. 221 (2018) 267–270, doi:10.1016/j.matlet.2018.03.156.

[44] G. Liu, C. Kang, J. Fang, L. Fu, H. Zhou, Q. Liu, MnO_2 nanosheet-coated Co_3O_4 complex for 1.4 V extra-high voltage supercapacitors electrode material, J. Power. Sources 431 (2019) 48–54, doi:10.1016/j.jpowsour.2019.05.053.

[45] Q. Cheng, C. Yang, K. Tao, L. Han, Inlaying ZIF-derived Co_3S_4 hollow nanocages on intertwined polypyrrole tubes conductive networks for high-performance supercapacitors, Electrochim. Acta 341 (2020) 136042, doi:10.1016/j.electacta.2020.136042.

[46] X. Zhao, H. Xu, Z. Hui, Y. Sun, C. Yu, J. Xue, R. Zhou, L. Wang, H. Dai, Y. Zhao, J. Yang, J. Zhou, Q. Chen, G. Sun, W. Huang, Electrostatically assembling 2D nanosheets of MXene and MOF - derivatives into 3D hollow frameworks for enhanced lithium storage, Small 15 (2019) 1904255, doi:10.1002/smll.201904255.

[47] M. Lan, X. Wang, R. Zhao, M. Dong, L. Fang, L. Wang, Metal-organic framework-derived porous $MnNi_2O_4$ microflower as an advanced electrode material for high-performance supercapacitors, J. Alloy. Comp. 821 (2020) 153546, doi:10.1016/j.jallcom.2019.153546.

[48] T. zhou, Z. Zang, J. Wei, J. Zheng, J. Hao, F. Ling, X. Tang, L. Fang, M. Zhou, Efficient charge carrier separation and excellent visible light photoresponse in Cu_2O nanowires, Nano. Energy 50 (2018) 118–125, doi:10.1016/j.nanoen.2018.05.028.

[49] J. Wei, Z. Zang, Y. Zhang, M. Wang, J. Du, X. Tang, Enhanced performance of light-controlled conductive switching in hybrid cuprous oxide/reduced graphene oxide (Cu_2O/rGO) nanocomposites, Opt. Lett. 42 (2017) 911–914, doi:10.1364/OL.42.000911.

[50] S.H.Kazemi F.Bahmani, Y. Wu, L. Liu, Y. Xu, Y. Lei, $CuMnO_2$-reduced graphene oxide nanocomposite as a free-standing electrode for high-performance supercapacitors, Chem. Eng. J. 375 (2019) 121966, doi:10.1016/j.cej.2019.121966.

[51] Y. Sui, A. Ye, J. Qi, F. Wei, Y. He, Q. Meng, Y. Ren, Z. Sun, Construction of $NiCo_2O_4$@$Ni_{0.85}Se$ core-shell nanorod arrays on Ni foam as advanced materials for an asymmetric supercapacitor, J. Alloy. Comp. 778 (2019) 234–238, doi:10.1016/j.jallcom.2018.10.354.

[52] Y. Xu, S. Hou, G. Yang, X. Wang, T. Lu, L. Pan, Synthesis of bimetallic $Ni_xCo_{1-x}P$ hollow nanocages from metal-organic frameworks for high performance hybrid supercapacitors, Electrochim. Acta 285 (2018) 192–201, doi:10.1016/j.electacta.2018.07.211.

[53] Y. Jiang, S. Zhang, Q. Ji, J. Zhang, Z. Zhang, Z. Wang, Ultrathin Cu_7S_4 nanosheets-constructed hierarchical hollow cubic cages: one-step synthesis based on Kirkendall effect and catalysis property, J. Mater. Chem. 2 (2014) 4574–4579, doi:10.1039/C3TA14838F.

[54] L. Liu, A. Liu, Y. Xu, F. Yang, J. Wang, Q. Deng, Z. Zeng, S. Deng, Fabrication of dual-hollow heterostructure of Ni_2CoS_4 sphere and nanotubes as advanced electrode for high-performance flexible all-solid-state supercapacitors, J. Colloid. Interf. Sci. 564 (2020) 313–321, doi:10.1016/j.jcis.2019.12.074.

[55] L. Abbasi, M. Arvand, S.E. Moosavifard, Facile template-free synthesis of 3D hierarchical ravine-like interconnected $MnCo_2S_4$ nanosheet arrays for hybrid energy storage device, Carbon 161 (2020) 299–308, doi:10.1016/j.carbon.2020.01.094.

[56] J. Lin, H. Jia, H. Liang, S. Chen, Y. Cai, J. Qi, C. Qu, J. Cao, W. Fei, J. Feng, Hierarchical $CuCo_2S_4$@NiMn-layered double hydroxide core-shell hybrid arrays as electrodes for supercapacitors, Chem. Eng. J. 336 (2018) 562–569, doi:10.1016/j.cej.2017.12.055.

[57] X. Wang, Y. Fang, B. Shi, F. Huang, F. Rong, R. Que, Three-dimensional $NiCo_2O_4$@$NiCo_2O_4$ core–shell nanocones arrays for high-performance supercapacitors, Chem. Eng. J. 334 (2018) 311–319, doi:10.1016/j.cej.2018.03.061.

[58] Y. Zhu, X. Ji, Z. Wu, Y. Liu, $NiCo_2S_4$ hollow microsphere decorated by acetylene black for high-performance asymmetric supercapacitor, Electrochim. Acta 186 (2015) 562–571, doi:10.1016/j.electacta.2015.10.176.

[59] J. Xu, S. Gai, F. He, N. Niu, P. Gao, Y. Chen, P. Yang, A sandwich-type three-dimensional layered double hydroxide nano-sheet array/graphene composite: fabrication and high supercapacitor performance, J. Mater. Chem. A 2 (2013) 1022–1031, doi:10.1039/c3ta14048b.

[60] D. Guo, X. Song, L. Tan, H. Ma, W. Sun, H. Pang, L. Zhang, X. Wang, A facile dissolved and reassembled strategy towards sandwich-like rGO@NiCoAl-LDHs with excellent supercapacitor performance, Chem. Eng. J. 356 (2019) 955–963, doi:10.1016/j.cej.2018.09.101.

[61] H. Xuan, Y. Guan, X. Han, X. Liang, Z. Xie, P. Han, Y. Wu, Hierarchical MnCo-LDH/rGO@$NiCo_2S_4$ heterostructures on Ni foam with enhanced electrochemical properties for battery-supercapacitors, Electrochim. Acta 335 (2020) 135691, doi:10.1016/j.electacta.2020.135691.

[62] Y. Chen, C. Jing, X. Fu, M. Shen, K. Li, X. Liu, H. Yao, Y. Zhang, K.X. Yao, Synthesis of porous NiCoS nanosheets with Al leaching on ordered mesoporous carbon for high-performance supercapacitors, Chem. Eng. J. 384 (2020) 123367, doi:10.1016/j.cej.2019.123367.

[63] M. Yan, Y. Yao, J. Wen, L. Long, M. Kong, G. Zhang, X. Liao, G. Yin, Z. Huang, Construction of Hierarchical $NiCo_2S_4$@PPy Core-shell heterostructure nanotubes array on Ni foam for high-performance asymmetric supercapacitor, ACS Appl. Mater. Interfaces 8 (2016) 24525, doi:10.1021/acsami.6b05618.

[64] I.I. Abu, K.J. Smith, The effect of cobalt addition to bulk MoP and Ni_2P catalysts for the hydrodes ulfurization of 4, 6-dimethyldibenzothiophene, J. Catal. 241 (2006) 356–366, doi:10.1016/j.jcat.2006.05.010.

[65] W. Chen, C. Xia, H.N. Alshareef, One-step electrodeposited nickel cobalt sulfide nano-sheet arrays for high-performance asymmetric supercapacitors, ACS. Nano 8 (2014) 9531–9541, doi:10.1021/nn503814y.
[66] H. Chen, J. Jiang, L. Zhang, T. Qi, D. Xia, H. Wan, Facilely synthesized porous $NiCo_2O_4$ flowerlike nanostructure for high-rate supercapacitors, J. Power. Sources 248 (2014) 28–36, doi:10.1016/j.jpowsour.2013.09.053.
[67] S.J. Patil, D.P. Dubal, D.W. Lee, Gold nanoparticles decorated rGO-$ZnCo_2O_4$ nanocomposite: a promising positive electrode for high performance hybrid supercapacitors, Chem. Eng. J. 379 (2020) 122211, doi:10.1016/j.cej.2019.122211.
[68] Z. Pan, F. Cao, X. Hu, X. Ji, A facile method for synthesizing CuS decorated Ti_3C_2 MXene with enhanced performance for asymmetric supercapacitors, J. Mater. Chem. A. 7 (2019) 8984–8992, doi:10.1039/C9TA00085B.
[69] N. Wang, B. Sun, P. Zhao, M. Yao, W. Hu, S. Komarneni, Electrodeposition preparation of $NiCo_2O_4$ mesoporous film on ultrafine nickel wire for flexible asymmetric supercapacitors, Chem. Eng. J. 345 (2018) 31–38, doi:10.1016/j.cej.2018.03.147.
[70] Y. Ouyang, R. Huang, X. Xia, H. Ye, X. Jiao, L. Wang, W. Lei, Hierarchical structure electrodes of NiO ultrathin nanosheets anchored to $NiCo_2O_4$ on carbon cloth with excellent cycle stability for asymmetric supercapacitors, Chem. Eng. J. 355 (2019) 416–427, doi:10.1016/j.cej.2018.08.142.
[71] H.B. Zhang, B. Xu, Z.Y. Xiao, H. Mei, L.L. Zhang, Y.F. Han, D.F. Sun, Optimizing crystallinity and porosity of hierarchical $Ni(OH)_2$ through conformal transformation of metal-organic framework template for supercapacitor applications, CrystEngComm 20 (2018) 4313–4320, doi:10.1039/C8CE00741A.
[72] C. Zhang, Z. Peng, Y. Chen, H. Chen, B. Zhang, H. Chen, J. Wang, M. Deng, Efficient coupling of semiconductors into metallic MnO_2@$CoMn_2O_4$ heterostructured electrode with boosted charge transfer for high-performance supercapacitors, Electrochim. Acta 347 (2020) 136246, doi:10.1016/j.electacta.2020.136246.
[73] Z. Zhang, H. Zhang, X. Zhang, D. Yu, Y. Ji, Q. Sun, Y. Wang, X. Liu, Facile synthesis of hierarchical $CoMoO_4$@$NiMoO_4$ core-shell nanosheet arrays on nickel foam as an advanced electrode for asymmetric supercapacitors, J. Mater. Chem. A 4 (2016) 18578–18584, doi:10.1039/C6TA06848K.
[74] P.R. Deshmukh, Y. Sohn, W.G. Shin, Electrochemical performance of facile developed aqueous asymmetric $(Fe,Cr)_2O_3$//MnO_2 supercapacitor, Electrochim. Acta 285 (2018) 381–392, doi:10.1016/j.electacta.2018.07.197.
[75] W.Q. Chen, J. Wang, K.Y. Ma, M. Li, S.H. Guo, F. Liu, J.P. Cheng, Hierarchical $NiCo_2O_4$@Co-Fe LDH core-shell nanowire arrays for high-performance supercapacitor, Appl. Surf. Sci. 451 (2018) 280–288, doi:10.1016/j.apsusc.2018.04.254.
[76] H. Chen, S. Chen, H. Shao, C. Li, M. Fan, D. Chen, G. Tian, K. Shu, Hierarchical $NiCo_2S_4$ nanotube@$NiCo_2S_4$ nanosheet arrays on Ni foam for high-performance supercapacitors, Chem. Asian. J. 11 (2016) 248–255, doi:10.1002/asia.201500972.